ELSEVIER

International Journal of Heat and Fluid Flow 22 (2001) 440–449

International Journal of HEAT AND FLUID FLOW

www.elsevier.com/locate/ijhff

Pressure distribution in laminar radial flow through inclined disks

F.C. Possamai [a], R.T.S. Ferreira [b], A.T. Prata [b,*]

[a] *Brazilian Compressor Industry, EMBRACO, Joinville, SC 89219-901, Brazil*

[b] *Department of Mechanical Engineering, Federal University of Santa Catarina, Caixa Postal – 476, Florianópolis, SC 88040-900, Brazil*

Received 8 December 1999; accepted 8 February 2001

Abstract

Experimentally validated numerical analysis of the incompressible laminar isothermal flow between concentric inclined disks has been performed. The flow is supplied axially by a feeding orifice placed in one of the disks and becomes radial after being deflected by the inclined frontal disk. The work represents a further step towards the understanding of the refrigerant flow through automatic valve systems in refrigerating compressors. The three-dimensional Navier–Stokes equation was written for an axially transformed non-orthogonal coordinate system and solved using the finite volume methodology. Coupling between pressure and velocity was handled through the SIMPLE algorithm and second-order interpolation schemes were employed to approximate the variables at the control volume faces. The numerical model was validated through direct comparison of experimental radial pressure profiles. The flow is significantly affected by the inclination of the frontal disk, even for inclinations as small as 0.1°. For some combinations of Reynolds number, gap distance and inclination between disks, the pressure distribution showed regions of negative values which tend to pull the frontal disk towards the valve seat and also produce a restoring moment tending to make the disks parallel.

Keywords: Radial flow; Radial diffuser; Compressor valve

1. Introduction

A large number of refrigerating compressors manufactured nowadays are reciprocating compressors where a linear reciprocating motion of a piston is responsible for increasing the refrigerant pressure. Usually, those compressors employ automatic valves that open and close due to the action of the flow. Those valves should have an adequate dynamic response, small pressure drop, and good performance in restricting gas back flow. Because of the major role that valve systems play in compressor efficiency, valve design is an important aspect of compressor technology.

The manner in which the fluid interacts with the valve movement is quite complex and very few attempts have been made to model this problem of solid–fluid interaction (Matos et al., 1999). Simplified models have been used to guide designers and to provide insights into the flow field and pressure distribution along the valve. In this regard, the flow through radial diffusers can be considered the basic problem for investigating automatic valves of reciprocating compressors.

Several investigators have studied radial flow observed in technological applications other than compressor valves. Among the various applications of radial flow one can cite thrust bearings, aerosol impactors, vertical take off and landing vehicles, and electro-erosion machining. The literature on radial flow is extensive and some representative contributions are due to Hayashi et al. (1975), Wark and Foss (1984), Ervin et al. (1989) and Tabatabai and Pollard (1987). For radial flow in the context of compressor valves the reader is referred to Ferreira and Driessen (1986), Prata and Ferreira (1990) and Prata et al. (1995).

More related to the present contribution are the works of Ferreira et al. (1989) and Gasche et al. (1992). In Ferreira et al. (1989), the pressure distribution in laminar radial flow through parallel concentric disks was investigated. Numerical solutions, experimentally validated, were presented for different gaps between disks and several Reynolds numbers. It was found that the pressure distribution on the frontal disk is very sensitive to the gap between the disks, especially for small gaps. A negative axial force contrary to the flow direction was found to develop on the frontal disk indicating that the frontal disk can be pulled towards the leeward disk. This is an undesirable effect in automatic valves since instead of opening because of the flow through it, the valve might close.

The paper by Gasche et al. (1992) extended the work of Ferreira et al. (1989) to eccentric disks. Although the eccentricity generated a three-dimensional and asymmetric flow, modifying considerably the pressure and velocity fields within the disks, the eccentricity did not alter significantly the resultant force on the frontal disk when compared to the concentric situation. Nevertheless, the different load distribution due to

* Corresponding author. Tel.: +55-48-234-5166; fax: +55-48-234-1519.

E-mail address: prata@nrva.ufsc.br (A.T. Prata).

0142-727X/01/$ - see front matter
PII: S0142-727X(01)00109-6

Notation

A_{ee}	effective flow area
A^*_{ee}	dimensionless effective flow area
A_{ef}	effective force area
A^*_{ef}	dimensionless effective force area
d	orifice diameter
D	reed diameter
F	force on the valve reed
F^*	dimensionless force on the valve reed
L	orifice length
$\dot{m}$	airflow rate
p	pressure
p^*	dimensionless pressure $[= 2p/\rho\overline{w}^2]$
p_{atm}	atmospheric pressure
p_u	pressure upstream the orifice
r, θ, z	cylindrical coordinates
r, θ, η	transformed coordinates
Re	Reynolds number based on the orifice diameter $[\rho\overline{w}d/\mu]$
s_c	displacement between the disks at centerline
T_u	temperature upstream the orifice
u, v, w	velocity components
$\overline{w}$	average velocity in the orifice

Greeks

α	valve reed inclination angle
δ	local distance between valve reed and valve seat
μ	air absolute viscosity
ρ	air density

eccentricity is important in evaluating the valve dynamic response.

The present work represents a further step towards the understanding of valve behavior. The geometry of the radial diffuser to be considered here is that of Fig. 1. As seen from the figure the flow is fed to the diffuser through an axial orifice. After being deflected by the frontal disk (valve reed) the flow becomes radial. In what follows, experiments and computations will be presented exploring the pressure distribution on the frontal disk as a function of the gap between the disks and the flow Reynolds number.

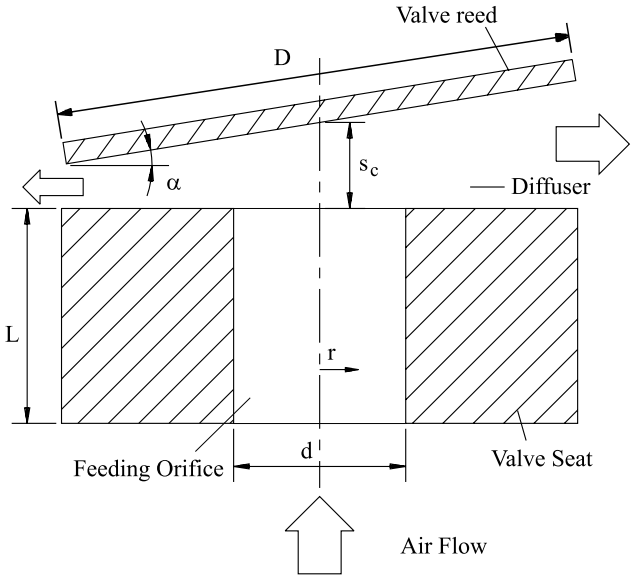

Fig. 1. Radial diffuser with inclined reed.

2. Experimental setup

A schematic view of the experimental setup is presented in Fig. 2. Compressed air stored in two reservoirs of 450 l each (maximum pressure of 1.2 MPa) was drawn into two horizontal aluminum tubes, each of length 2 m and mounted in series. Between the two tubes an orifice flow meter was installed. A control valve was placed at the entrance of the first aluminum tube and allowed an accurate adjustment of the flow rate.

At the exit of the second aluminum tube the air reached the test section. The length to diameter ratio of the tubes larger than 50 assured a fully developed flow at both the test section and the orifice flow meter. A pressure tap close to the entrance of the test section was used to measure the static pressure required to determine the air density used for the data reduction.

As illustrated in Fig. 3(a), the test section consisted of a radial diffuser, a system for positioning the frontal disk (valve reed) and equipments for measuring the gap between the reed and the valve seat, as well as the reed inclination. Prior to reaching the diffuser, the flow entered a feeding orifice whose diameter was equal to the diameter of the aluminum tube. The ratio between the reed diameter and the diameter of the

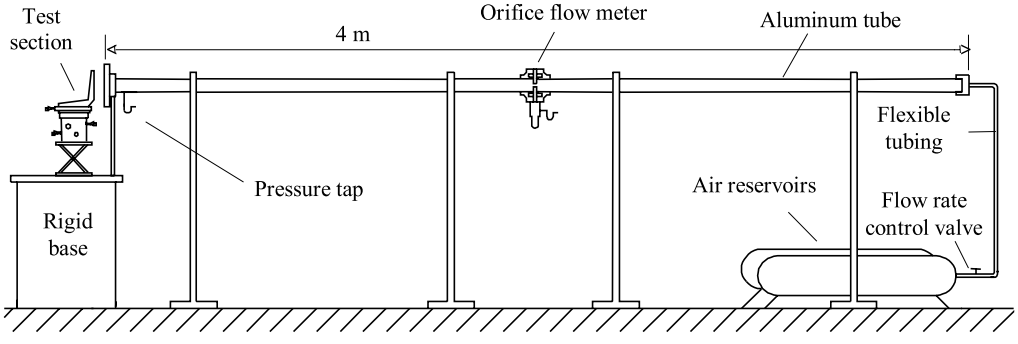

Fig. 2. Schematic view of experimental aparatus.

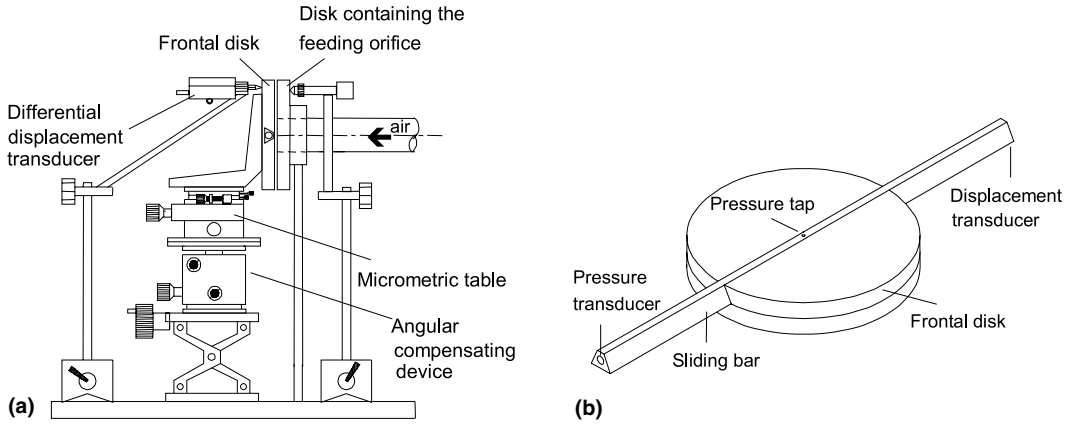

Fig. 3. Details of test section. (a) Test section and positioning system, (b) valve reed (frontal disk) with sliding bar.

Table 1
Modification of the distance between the disks due to the flow induced force

$s_c/d = 0.012$					
Re	1004	1505	2008	2505	3000
s_{cor} (μm)	11	15	17	20	22
$s_c/d = 0.020$					
Re	997	1502	2003	2500	3006
s_{cor} (μm)	2	3	4	4	5

feeding orifice was kept constant for all runs and equal to $D/d = 3$.

The valve seat and reed have both the same diameter of 104.7 mm. Except for the valve reed, which was made of stainless steel, all other pieces were made of aluminum. Because of the major focus of the present work on the pressure distribution on the valve reed, special care was taken on designing and machining this piece. A sliding bar provided with a small tap hole (0.7 mm diameter) and an internal connecting perforation (2 mm diameter) was inserted along the reed diameter, according to Fig. 3(b). Petroleum jelly was employed to seal and to lubricate the surfaces of the bar. At one end of the bar an inductive displacement transducer was placed to allow the accurate location of the pressure tap. At the other end a pressure transducer collected the pressure signal. Both pressure and location data were fed into a data acquisition system.

Micrometric tables were used to locate the valve reed with respect to the valve seat. The pressure distribution along the reed is very sensitive to the distance between the diffuser disks. For the Reynolds number of 1512, based on the diameter of the feeding orifice, and $s_c/d = 0.012$, for example, a variation of 9 μm in the gap between the disks caused a 8% variation on the stagnation pressure. Because of the aforementioned sensitivity of the flow field with the diffuser geometry, even deformations of the positioning system due to the flow induced pressure on the reed had to be taken into account. Typical values of the corrections in the distance between the disks, s_{cor} associated with the flow induced deformation is presented in Table 1. For all cases in Table 1 the disks were kept parallel.

3. Experimental procedures

At the beginning of each experimental run the first step was to clean with benzene the surfaces of the valve reed and seat. Next, the reed was positioned at a desired location. The first adjustments concerned parallelism and concentricity of the disks. This was performed using a steel sphere with diameter of 3.9712 ± 0.0008 mm glued to a fine thread. The sphere was passed along the gap between the disks, and the micrometric tables were adjusted.

Next, a sample data acquisition was processed and through a visual observation of the symmetry of the pressure profile along the reed, the disks parallelism and concentricity were checked. After being centered, the reed was inclined to a desired angle. A new adjustment was then required to center the reed since the angular displacement altered the position of the reed center line. The reference zero gap between disks was determined using the known diameter of the steel sphere.

To initiate the experimental run the control valve was adjusted to yield the desired Reynolds number. Then the sliding bar was moved and a preliminary pressure data were taken to

Table 2
Typical values of the variables measured in each experimental run, with their uncertainty, respectively

Variable	Typical value	Uncertainty	Uncertainty (%)
p_u (Pa)	117.63	1.92	1.633
T_{amb} (K)	292.15	0.50	0.171
p_{atm} (Pa)	102137	66	0.065
ρ (kg/m^3)	1.219	0.002	0.164
μ (Pa s)	1.82×10^{-5}	2.40×10^{-8}	0.132
$\dot{m}$ (kg/s)	9.96×10^{-4}	2.65×10^{-6}	0.266
$\overline{w}$ (m/s)	0.854	0.003	0.308
p (Pa)	125.26	0.39	0.311
p^*	282.9	1.9	0.707
Re	1997	6	0.266
s_c (μm)	698	10	1.43
α (°)	0.2	0.006	3.0

obtain the maximum and minimum values that were used to set the proper scale for the plot of pressure versus radial position that would appear on the computer screen. The sliding bar was then returned to its initial location with the pressure tap at the reed rim. At this point everything was ready for the data run, and the sliding bar was carefully moved from one side to the other at a constant speed of approximately 10 mm/s. If the pressure plot registered in the computer screen was satisfactory, the run was ended and the data reduction was performed.

For each experimental run an uncertainty analysis was executed following the methodology described by Moffat (1982). Typical uncertainty values for $Re = 1997$, $s_c/d = 0.02$ and $\alpha = 0.2$ are presented in Table 2.

4. Problem formulation

The governing equations for the problem being considered here will be obtained with the aid of Fig. 1. The basic assumptions to be made are isothermal and incompressible steady flow for a Newtonian fluid. From Fig. 1 it is seen that because of the reed inclination the fluid tends to flow through the region of higher gap between the disks generating velocity gradients along the circumferential direction. That makes the flow three-dimensional and due to the reed inclination non-orthogonal coordinates are the natural choice. Orthogonal coordinates have the advantage of using fewer terms in the governing equations but the reproduction of irregular boundaries can only be achieved by approximations (Sparrow and Prata, 1983; Prata and Sparrow, 1984). Here non-orthogonal coordinates are employed and the physical domain is transformed to the computational domain following the practice described in Faghri et al. (1984). Along the axial direction a new coordinate is introduced, η, so that,

$$\eta = z/\delta(r,\theta), \quad 0 \leqslant \eta \leqslant 1, \tag{1}$$

where $\delta(r,\theta)$ is the local distance between the valve seat and valve reed, given by

$$\delta(r,\theta) = s_c - r\tan\alpha\cos\theta. \tag{2}$$

The effect of this coordinate transformation is illustrated in Fig. 4.

The introduction of the η coordinate replacing z in the cylindrical version of the Navier–Stokes equation yields numerous new terms as seen in Appendix A. At this point it should be noted that for the application considered here the inclination angle is small. For the present work the maximum inclination to be considered is 0.9°; and as will be seen later, even that small value has a strong impact on the flow field within the disks.

For small α value a simplified version of the equations presented in Appendix A can be used with little effect on the accuracy of the model. This simplified version ignores the terms containing $\partial\eta/\partial r$ and $\partial\eta/\partial\theta$, and retains only those containing $\partial\eta/\partial z = 1/\delta(r,\theta)$. Therefore, all terms having A_1, A_2 and C_2 in Eqs. (A.1)–(A.4) are dropped and the working equations for the problem become,

Continuity:

$$\frac{\partial}{\partial\theta}(\rho u) + \frac{\partial}{\partial r}(\rho r v) + \frac{1}{\delta}\frac{\partial}{\partial\eta}(\rho r w) = 0. \tag{3}$$

Momentum in θ direction:

$$\begin{aligned}\frac{1}{r}\left[\frac{\partial}{\partial\theta}(\rho u u) + \frac{\partial}{\partial r}(\rho r v u) + \frac{1}{\delta}\frac{\partial}{\partial\eta}(\rho r w u)\right] &= -\frac{1}{r}\frac{\partial p}{\partial\theta} + \frac{\mu}{r}\left[\frac{\partial}{\partial\theta}\left(\frac{1}{r}\frac{\partial u}{\partial\theta}\right) + \frac{\partial}{\partial r}\left(r\frac{\partial u}{\partial r}\right)\right.\\ &\left. + \frac{1}{\delta}\frac{\partial}{\partial\eta}\left(\frac{r}{\delta}\frac{\partial u}{\partial\eta}\right)\right] + \frac{2\mu}{r^2}\frac{\partial v}{\partial\theta} - \frac{\mu u}{r^2} - \frac{\rho u v}{r}.\end{aligned} \tag{4}$$

Momentum in r direction:

$$\begin{aligned}\frac{1}{r}\left[\frac{\partial}{\partial\theta}(\rho u v) + \frac{\partial}{\partial r}(\rho r v v) + \frac{1}{\delta}\frac{\partial}{\partial\eta}(\rho r w v)\right] &= -\frac{\partial p}{\partial r} + \frac{\mu}{r}\left[\frac{\partial}{\partial\theta}\left(\frac{1}{r}\frac{\partial v}{\partial\theta}\right) + \frac{\partial}{\partial r}\left(r\frac{\partial v}{\partial r}\right) + \frac{1}{\delta}\frac{\partial}{\partial\eta}\left(\frac{r}{\delta}\frac{\partial v}{\partial\eta}\right)\right]\\ &- \frac{2\mu}{r^2}\frac{\partial u}{\partial\theta} - \frac{\mu v}{r^2} + \frac{\rho u^2}{r}.\end{aligned} \tag{5}$$

Momentum in η direction:

$$\begin{aligned}\frac{1}{r}\left[\frac{\partial}{\partial\theta}(\rho u w) + \frac{\partial}{\partial r}(\rho r v w) + \frac{1}{\delta}\frac{\partial}{\partial\eta}(\rho r w w)\right] &= -\frac{1}{\delta}\frac{\partial p}{\partial\eta} + \frac{\mu}{r}\left[\frac{\partial}{\partial\theta}\left(\frac{1}{r}\frac{\partial w}{\partial\theta}\right) + \frac{\partial}{\partial r}\left(r\frac{\partial w}{\partial r}\right)\right.\\ &\left. + \frac{1}{\delta}\frac{\partial}{\partial\eta}\left(\frac{r}{\delta}\frac{\partial w}{\partial\eta}\right)\right].\end{aligned} \tag{6}$$

The non-orthogonal coordinate η is employed only in the diffuser region. In the orifice δ is made equal to 1 and the cylindrical coordinate system is recovered.

Boundary conditions for Eqs. (3)–(6) are of three types: solid walls, inflow and outflow. At the solid walls the non-slip and impermeable boundary condition are imposed, that is, $u = v = w = 0$. At the outflow a parabolic boundary

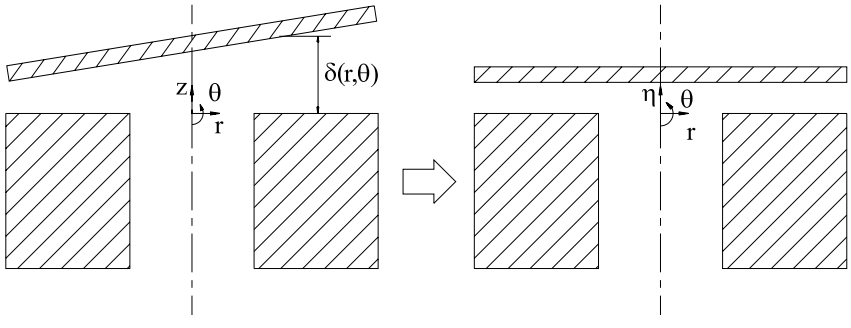

Fig. 4. Physical and computational domain.

condition is imposed, that is, $w = \partial u/\partial r = \partial(rv)/\partial r = 0$. For the Reynolds numbers considered here separation always occurred as the fluid turned from the feeding orifice to the diffuser section, Fig. 1. At larger inclination between the disks, the separation region extended beyond the diffuser exit. For those cases, further tests showed that even though the prescribed boundary conditions introduced some minor distortions on the streamline curvatures at the outflow, the pressure distribution along the valve remained unaltered when higher-order approximations were employed for the boundary conditions at the diffuser exit. Further tests were carried out extending the computation domain beyond the diffuser exit and again the pressure results showed no variation. All that, together with the favorable comparisons with the experiments, yielded confidence on the outflow boundary condition adopted.

A further condition is required to ensure that ambient pressure is obtained at the diffuser exit; since the continuity equation is used as a pressure equation in the methodology to be described in the next section, for that equation the pressure was made equal to zero at the diffuser exit.

For the inflow it was recognized, as discussed by Ferreira et al. (1989), that due to the small value of s_c/d for valve applications, the fluid is strongly accelerated close to the orifice wall in order to enter the diffuser. Due to this throttling the specification of the inflow velocity profile plays no role in the solution of the flow field in the diffuser (Ferreira et al., 1989). Thus, the inflow boundary condition was $u = v = 0$ and $w = \overline{w} = \mu Re/\rho d$.

5. Solution methodology

A finite volume discretization scheme was used here to solve the governing differential equations. According to this practice the solution domain is divided into small non-overlapping control volumes and the continuity and momentum differential equations are integrated over each control volume (Patankar, 1980; Ferziger and Peric, 1996). The resulting system of algebraic equations is solved using a combination of the Thomas algorithm and the Gauss–Seidel method (see Patankar, 1980). Prior to solving the algebraic system of equations the discretized form of the continuity equation was transformed into an equation for pressure using the SIMPLE methodology (Patankar, 1980).

A key issue in the accuracy of the numerical solution is the interpolation scheme employed to evaluate the variables at the control volume faces. Here the QUICK scheme as presented by Hayase et al. (1992) was adopted, yielding a second-order accuracy for the interpolated values. In some cases numerical instabilities introduced by the QUICK methodology precluded convergence. Even though a consistent QUICK scheme was used here, those instabilities were only eliminated when the power-law scheme of Patankar (1980) was employed in the axial and circumferential directions. As observed from several numerical experiments performed, the radial direction is the most critical for the numerical accuracy of the solution, and the second-order interpolation scheme was maintained for that direction.

Due to the strong non-linearity of the equations, under relaxation coefficients were required. For the velocity components these coefficients were 0.2 and for pressure 0.4. Convergence was stopped when the maximum residual of the algebraic equations was less than 10^{-6}; at the beginning of the computations the value of the maximum residual was 10^{-1}. All results to be presented were obtained with a mesh consisted of $16 \times 60 \times 43 = 41{,}280$ grid points (circumferential $\times$ radial $\times$ axial). All points were hand placed with higher concentration in the regions of steeper gradients. The final mesh adopted in performing the computations was chosen after several grid independence tests were carried out. In Section 6 the accuracy of the numerical results and the adequacy of the chosen mesh will be addressed.

6. Numerical uncertainty

The numerical model was first validated through comparisons with analytical results for limiting cases. For low Reynolds numbers and small gaps between the disks, inertial effects can be neglected when compared with viscous effects. Under these circumstances, analytical solution for parallel disks can be obtained. The dimensionless pressure along the diffuser is then given by

$$p^* = 2p/(\rho\overline{w}^2) = \frac{3\ln[(0.5(D/d)/(r/d)]}{Re(s_c/d)^3}, \tag{7}$$

where all variables are defined in the nomenclature. Comparisons between analytical and numerical results for $Re = 70$ and $s_c/d = 0.01$ yielded maximum deviations of 2% in the p^* values.

For higher values of Reynolds numbers, inertial effects should be considered and an analytical solution of the pressure distribution along the diffuser is not possible. For those situations, which are the ones explored in the present work, a quantitative assessment of the uncertainty of the computational results was obtained based on the methodology described in Roache (1993) and Demuren and Wilson (1993). Results obtained with the mesh consisted of $16 \times 60 \times 43$ grid points (circumferential $\times$ radial $\times$ axial) were compared with those obtained with a more refined mesh in which the number of grid points was doubled along each coordinate direction, that is, $32 \times 120 \times 86$ (circumferential $\times$ radial $\times$ axial). Having the pressure field calculated using a fine grid and a coarse grid, Richardson extrapolation was employed to evaluate what would be the exact pressure field as recommended by Roache (1993). The formula for the exact solution based on the fine and the coarse grid also requires that the order of the numerical scheme be estimated. As previously discussed, a second-order accuracy interpolating scheme was employed for most of the computations explored here. However, because in some cases use was made of the power-law scheme, in performing the grid sensitivity tests this scheme was employed and its order was considered to be equal to one. This was a conservative approach as discussed by Demuren and Wilson (1993).

Results for the pressure distribution along the valve reed are presented in Fig. 5 for both the fine and coarse grids as well as the extrapolated exact results. For the case depicted in the figure $Re = 1000$, $s_c/d = 0.0120$ and $\alpha = 0.1°$. The main features of the pressure distribution along the valve will be discussed further. At this moment attention should be focused on the comparisons among the solutions. Except for $r/d \approx -0.5$ where large deviations occur between the extrapolated exact solution and the coarse grid solution, overall a good agreement prevailed. Close to the $r/d \approx -0.5$ region, strong gradients preclude a better accuracy of the computations and that was somehow expected. At the plateau, the deviation between the extrapolated exact solution and the coarse grid solution was 2.4%.

A further validation of both numerical and experimental results was performed through comparisons between the two. These comparisons will be explored in the following sections.

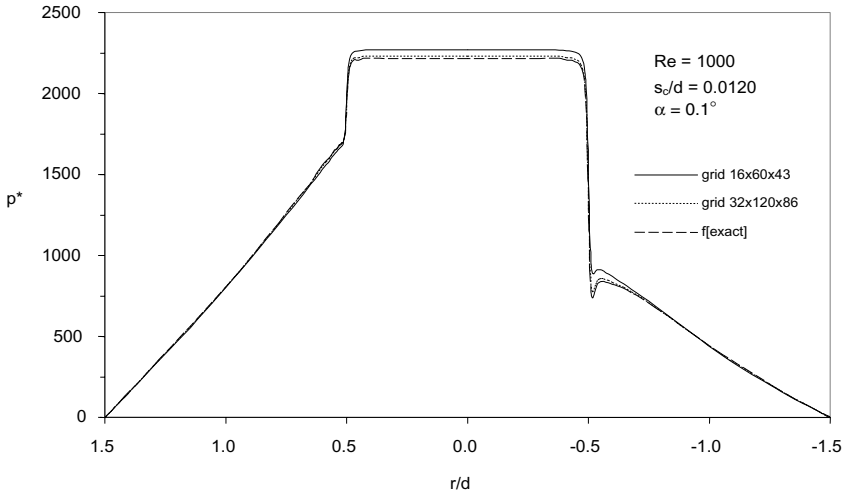

Fig. 5. Grid sensitivity results for pressure distribution along valve reed for $Re = 1000, s_c/d = 0.0120$ and $\alpha = 0.1°$.

7. Results and discussions

In the results to be presented, three parameters were varied: Reynolds number, gap between disks and inclination of the valve reed. The Reynolds numbers were varied from 500 to 2500, three gaps were explored, 0.01, 0.02 and 0.03, and the inclination angle was varied from 0° to 0.9°. At the entrance of the diffuser proper, the Reynolds number based in the gap between the disks, Re_s, is four times smaller than Re based on the orifice diameter. As r increases along the diffuser, Re_s, decreases assuring that for the range of Re investigated here the flow was laminar throughout the diffuser.

8. Pressure distribution

The main focus of the present work is on the pressure distribution along the valve reed. In this regard Figs. 6 and 7 were prepared. Those figures present both experimental and numerical results. The nominal distance between disks of 0.012 at the axis line is explored in Fig. 6 for $\alpha = 0°$ and 0.2°. For each angle two nominal Reynolds numbers are considered, $Re = 1500$ and 2000. The circumferential coordinate, θ, starts at the location where $\delta(r, \theta)$ has its minimum value and all pressure profiles to be explored next are plotted along the valve reed diameter that comprises the $\theta = 0$ and π coordinates.

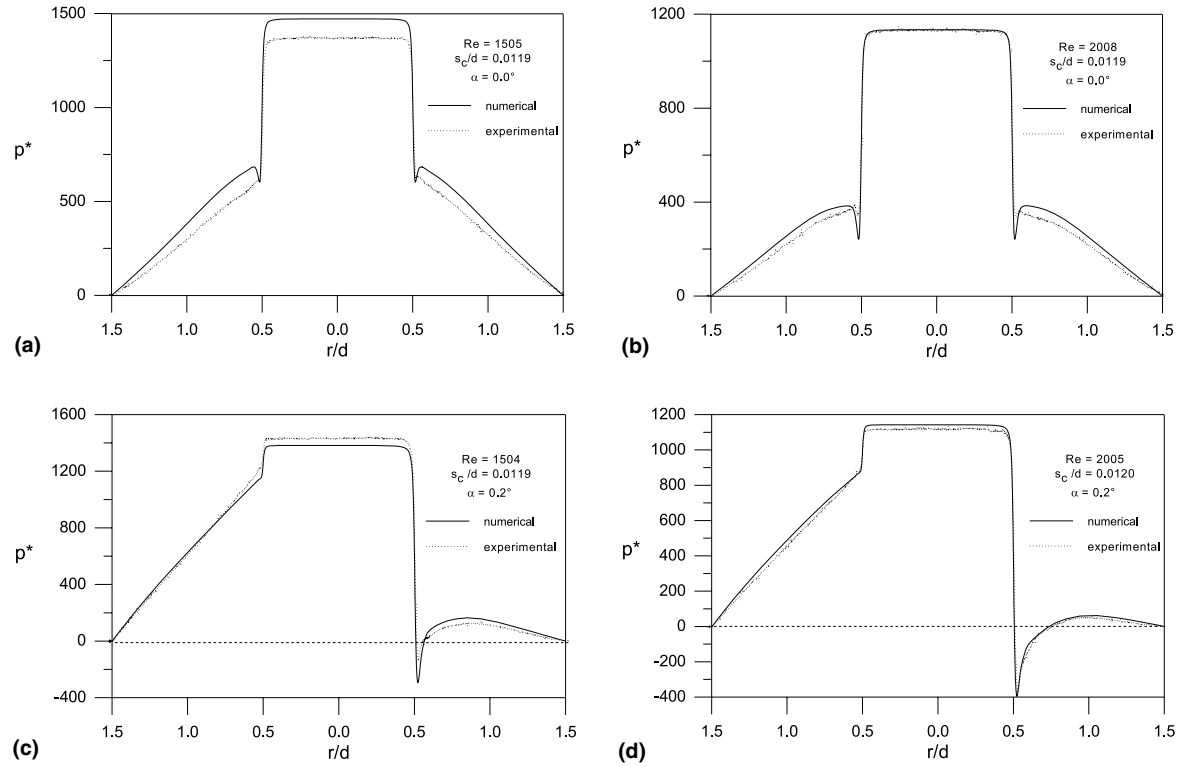

Fig. 6. Numerical and experimental results for pressure distribution along valve reed for $s_c/d = 0.012$. (a) $\alpha = 0°, Re = 1505$, (b) $\alpha = 0°, Re = 2008$, (c) $\alpha = 0.2°, Re = 1504$, (d) $\alpha = 0.2°, Re = 2005$.

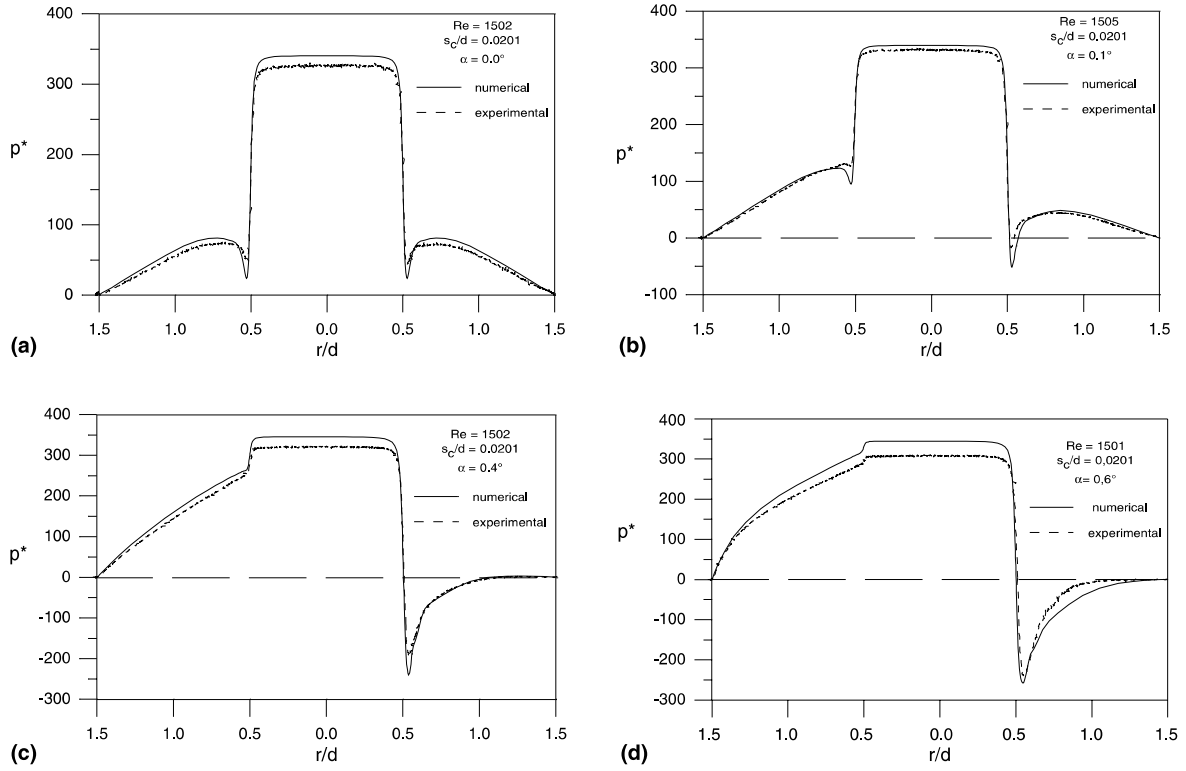

Fig. 7. Numerical and experimental results for pressure distribution along valve reed for $Re = 1500$ and $s_c/d = 0.02$. (a) $\alpha = 0°, Re = 1502$, (b) $\alpha = 0.1°, Re = 1505$, (c) $\alpha = 0.4°, Re = 1502$, (d) $\alpha = 0.6°, Re = 1501$.

Several aspects are observed in those figures. The main characteristic of the pressure profiles is the plateau for $r/d \leqslant 0.5$. The occurrence of the plateau is due to the stagnation region at the end of the feeding orifice prior to the fluid entering the region between the disks. For $\alpha = 0°$ the pressure distribution is symmetric with respect to the axial line. This is not the case for other values of α, and the flow asymmetry increases with increasing inclination.

Due to the small distance between the disks compared to the orifice diameter, a strong pressure drop is observed at the diffuser entrance. As observed in early works (see for example Ferreira et al., 1989) the abrupt pressure decay at the diffuser entrance is stronger for higher Re and s_c/d values. This decay can be so strong that negative pressures might occur as seen in the figures. Despite the strong acceleration of the fluid particles as they turn from the feeding orifice and enter the diffuser, the corresponding pressure decay was captured by both experiments and computations, and a reasonable to good agreement prevailed between the results.

The inclination of the valve reed plays an important role on the pressure distribution within the diffuser. Even a small inclination of $\alpha = 0.1°$ (shown in Fig. 7(b)), can completely destroy the circumferential symmetry. Another aspect worth noting is the good agreement between computation and experiments which validated both the numerical model and the experimental setup. In considering the agreement it should be recalled that a variation of 9 μm in the s_c value caused a 8% variation on the stagnation pressure for $Re = 1512$ and $s_c/d = 0.012$, as mentioned before.

In Fig. 7 results for pressure distribution along the valve reed were presented for nominal values of $Re = 1500$ and $s_c/d = 0.02$. From this figure becomes more clear the effect of reed inclination on the pressure. The region of higher pressure corresponds to the part of the reed that is closer to

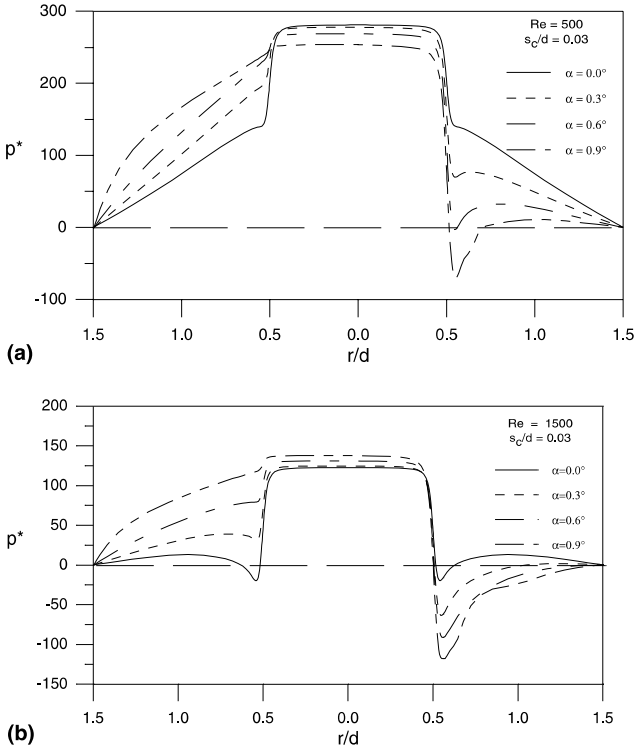

Fig. 8. Numerical results for pressure distribution along valve reed for $s_c/d = 0.03$. (a) $Re = 500$, (b) $Re = 1500$.

the valve seat. As seen from Fig. 7, for $\alpha = 0.6°$ the pressure pattern is completely altered because of the inclination. For the left-hand side of the figure the pressure profile is typical of a flow where viscous effects are dominant whereas the right-hand side indicates a strong influence of inertial effects.

The previous results yielded confidence on the numerical model and allowed other results to be obtained. Fig. 8 presents, for $s_c/d = 0.03$, numerical results for the pressure distribution along the valve having the inclination as a curve parameter. Fig. 8(a) is for $Re = 500$ and Fig. 8(b) for $Re = 1500$. An important effect associated with the asymmetry of the pressure distribution on the reed due to the inclination is a restoring moment that tends to align the valve reed. This moment resulted from the combination of an outward force in the region where the reed is closer to the seat and an inward force in the region where the reed is more distant from the seat. The restoring moment is very beneficial to the valve operation because it tends to maintain both reed and seat aligned.

In order to provide a pictorial view of the pressure distribution on the valve reed, Fig. 9 was prepared. From this figure can be seen the circumferential variation of the pressure on the reed. Also emphasized by the figure is the stagnation region as well as the abrupt pressure decay associated with the flow entrance in the radial diffuser.

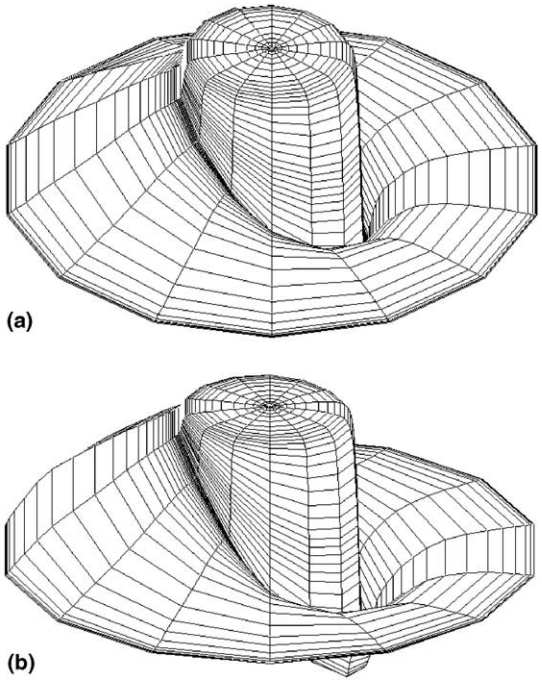

Fig. 9. Pressure distribution on valve reed for $Re = 1500$ and $s_c/d = 0.02$. (a) $\alpha = 0.4$, (b) $\alpha = 0.6°$.

9. Force on the valve reed

The integration of the local pressure on the reed along its surface yielded the total force on the valve. Results for the dimensionless force $F^*(= 2F/\rho\overline{w}^2d^2)$ are given in Fig. 10 for $s_c/d = 0.01$ and 0.03. For each gap two Reynolds numbers are considered, $Re = 500$ and 1500. Because the dimensionless force has an average velocity raised to the square in the denominator, the F^* values for $Re = 500$ are higher than those for $Re = 1500$. It should be noted, however, that the dimensional force on the reed increases with increasing values of Re.

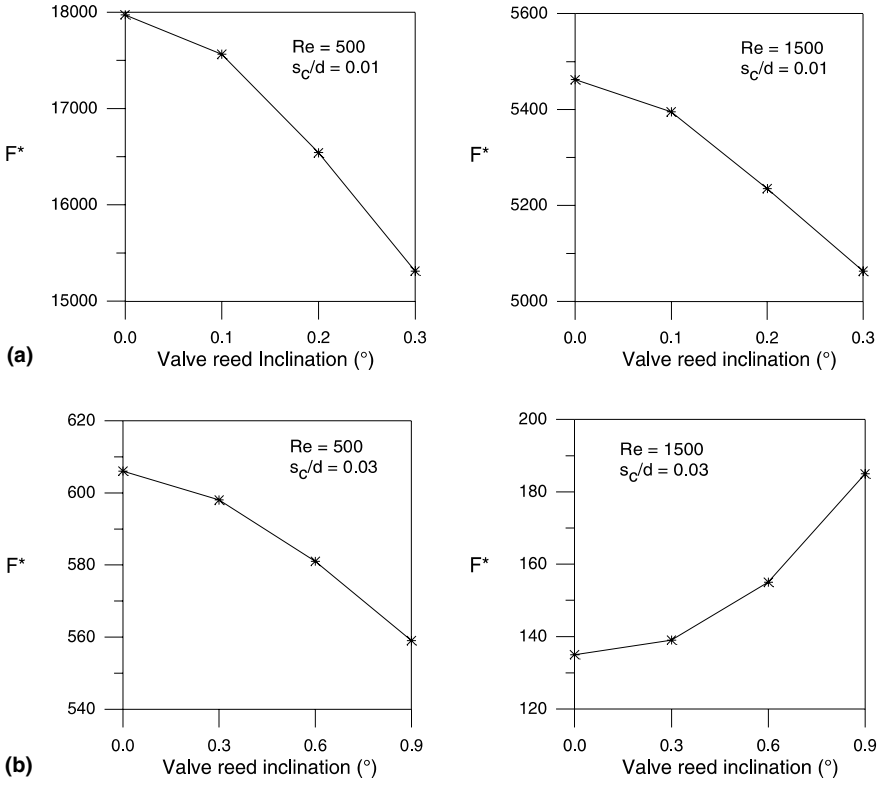

Fig. 10. Dimensionless force on valve reed. (a) $s_c/d = 0.01$, (b) $s_c/d = 0.03$.

Table 3
Dimensionless effective flow area

α	A^*_{ee}			
	$s_c/d = 0.01$		$s_c/d = 0.03$	
	$Re = 500$	$Re = 1500$	$Re = 500$	$Re = 1500$
0.0	0.0121	0.0200	0.0598	0.0908
0.1	0.0122	0.0201	0.0599	0.0906
0.2	0.0127	0.0205	0.0600	0.0904
0.3	0.0134	0.0211	0.0602	0.0902
0.6	–	–	0.0612	0.0878
0.9	–	–	0.0629	0.0857

Table 4
Dimensionless effective flow area

α	A^*_{ee}			
	$s_c/d = 0.01$		$s_c/d = 0.03$	
	$Re = 500$	$Re = 1500$	$Re = 500$	$Re = 1500$
0.0	3.35	2.80	2.77	1.42
0.1	3.36	2.80	2.77	1.42
0.2	3.40	2.81	2.76	1.43
0.3	3.51	2.89	2.76	1.44
0.6	–	–	2.77	1.52
0.9	–	–	2.83	1.72

For small values of s_c/d the force on the reed decreases as α increases. This tendency is inverted for higher values of s_c/d and for $s_c/d = 0.03$ and $\mathrm{Re} = 1500$ the force increases with increasing values of α.

10. Parameter efficiency

Two parameters are very important in the valve design: the effective flow and force areas. Those two parameters are generally used in numerical simulation of compressors and can also be used to evaluate the efficiency of the valves.

The effective flow area, A_{ee} is related to the pressure drop through the valve. For a given pressure drop A_{ee} can yield the mass flux across the valve. Thus, the higher the A_{ee} the better the valve performance with respect to the flow through it. The effective flow area was defined as

$$A_{ee} = \frac{\dot{m}}{p_u \sqrt{\frac{2k}{(k-1)RT_u}} \sqrt{r^{2/k} - r^{(k+1)/k}}}, \tag{8}$$

where except for $r = p_{atm}/p_u$ and $k = c_p/c_v$ all other quantities are defined in the nomenclature.

Results for dimensionless $A^*_{ee}(= A_{ee}/d^2)$ are shown in Table 3 for $s_c/d = 0.01$ and 0.03. As seen from the table, α for $s_c/d = 0.03$ and $Re = 1500$, the same pressure drop results in lesser mass flow rate as the inclination increases.

The flow induced force in computing the valve movement in compressor simulation programs is usually obtained via the effective force area, A_{ef}. From the pressure difference across the valve, Δp_v, A_{ef} is determined from $A_{ef} = F/\Delta p_v$. Values of the dimensionless $A^*_{ef}(= A_{ef}/d^2)$ for various A^*_{ee} tends to increase as α increases, but as a function of s_c/d and Re are shown in Table 4. For all cases investigated A_{ef} increased with increasing values of α. A further discussion about valve geometric parameters on the effective force and flow areas can be found in Ferreira and Driessen (1986).

11. Conclusions

The present work presented a numerical and an experimental investigation of the incompressible laminar and isothermal flow in a radial diffuser having one disk inclined with respect to the other. This configuration represents the basic flow problem associated with automatic valves of reciprocating compressors. A very good agreement prevailed between computation and experimental results validating both the numerical methodology and the experiments. From the experimental and numerical results it was found that the flow field is very sensitive to the inclination between the disks. For an inclination angle as small as 0.1° the pressure distribution symmetry associated to the parallel situation was destroyed. The higher the Reynolds number and the distance between the disks, the greater the impact of the inclination on the asymmetry of the pressure field. An important effect associated with the asymmetry of the pressure distribution on the reed is the occurrence of a restoring moment that tends to align the two disks. This moment originates from the combination of an outward force in the region where the disks are closer and an inward force in the region where the disks are apart.

Acknowledgements

This work is part of a technical-scientific cooperation program between Federal University of Santa Catarina and the Brazilian Compressor Industry, EMBRACO. Partial support from the Brazilian Research Council, CNPq, is also appreciated.

Appendix A

Full Navier–Stokes equation in, θ r and η coordinates:

θ direction:

$$\frac{1}{r}\left[\frac{\partial}{\partial\theta}(\rho uu)+\frac{\partial}{\partial r}(\rho rvu)+\frac{1}{\delta}\frac{\partial}{\partial\eta}(\rho rwu)\right] = -\frac{1}{r}\frac{\partial p}{\partial\theta}+\frac{\mu}{r}\left[\frac{\partial}{\partial\theta}\left(\frac{1}{r}\frac{\partial u}{\partial\theta}\right)+\frac{\partial}{\partial r}\left(r\frac{\partial u}{\partial r}\right) +\frac{1}{\delta}\frac{\partial}{\partial\eta}\left(\frac{r}{\delta}\frac{\partial u}{\partial\eta}\right)\right]+\frac{2\mu}{r^2}\frac{\partial v}{\partial\theta}-\frac{\mu u}{r^2}-\frac{\rho uv}{r}-A_1\frac{\partial}{\partial\eta}(\rho uv) +\frac{A_2}{r}\frac{\partial}{\partial\eta}(\rho uu)-\mu\left[-\frac{1}{r}\frac{\partial}{\partial r}\left(A_1 r\frac{\partial u}{\partial\eta}\right)-A_1\frac{\partial}{\partial\eta}\left(\frac{\partial u}{\partial r}\right) +\frac{A_1^2}{\eta}\frac{\partial}{\partial\eta}\left(\eta\frac{\partial u}{\partial\eta}\right)+\frac{1}{r^2}\frac{\partial}{\partial\theta}\left(A_2\frac{\partial u}{\partial\theta}\right)+\frac{A_2}{r^2}\frac{\partial}{\partial\eta}\left(\frac{\partial u}{\partial\theta}\right) +\frac{1}{r^2}C_2^2\sin^2\theta\frac{\partial}{\partial\eta}\left(\eta\frac{\partial u}{\partial\eta}\right)\right]+\frac{A_2}{r}\frac{\partial p}{\partial\eta}-\frac{2\mu A_1}{r^2}\frac{\partial v}{\partial\eta}. \tag{A.1}$$

r direction:

$$\frac{1}{r}\left[\frac{\partial}{\partial\theta}(\rho uv)+\frac{\partial}{\partial r}(\rho rvv)+\frac{1}{\delta}\frac{\partial}{\partial\eta}(\rho rwv)\right] = -\frac{\partial p}{\partial r}+\frac{\mu}{r}\left[\frac{\partial}{\partial\theta}\left(\frac{1}{r}\frac{\partial v}{\partial\theta}\right)+\frac{\partial}{\partial r}\left(r\frac{\partial v}{\partial r}\right) +\frac{1}{\delta}\frac{\partial}{\partial\eta}\left(\frac{r}{\delta}\frac{\partial v}{\partial\eta}\right)\right]-\frac{2\mu}{r^2}\frac{\partial u}{\partial\theta}-\frac{\mu v}{r^2}+\frac{\rho u^2}{r}-A_1\frac{\partial}{\partial\eta}(\rho vv) +\frac{A_2}{r}\frac{\partial}{\partial\eta}(\rho uv)-\mu\left[-\frac{1}{r}\frac{\partial}{\partial r}\left(A_1 r\frac{\partial v}{\partial\eta}\right)-A_1\frac{\partial}{\partial\eta}\left(\frac{\partial v}{\partial r}\right) +\frac{A_1^2}{\eta}\frac{\partial}{\partial\eta}\left(\eta\frac{\partial v}{\partial\eta}\right)+\frac{1}{r^2}\frac{\partial}{\partial\theta}\left(A_2\frac{\partial v}{\partial\theta}\right)+\frac{A_2}{r^2}\frac{\partial}{\partial\eta}\left(\frac{\partial v}{\partial\theta}\right) +\frac{A^2}{r^2\eta}\frac{\partial}{\partial\eta}\left(\eta\frac{\partial v}{\partial\eta}\right)\right]-A_1\frac{\partial p}{\partial\eta}+\frac{2\mu A_2}{r^2}\frac{\partial v}{\partial\eta}. \tag{A.2}$$

η direction:

$$\frac{1}{r}\left[\frac{\partial}{\partial\theta}(\rho uw)+\frac{\partial}{\partial r}(\rho rvw)+\frac{1}{\delta}\frac{\partial}{\partial\eta}(\rho rww)\right] = -\frac{1}{\delta}\frac{\partial p}{\partial\eta}+\frac{\mu}{r}\left[\frac{\partial}{\partial\theta}\left(\frac{1}{r}\frac{\partial w}{\partial\theta}\right)+\frac{\partial}{\partial r}\left(r\frac{\partial w}{\partial r}\right) +\frac{1}{\delta}\frac{\partial}{\partial\eta}\left(\frac{r}{\delta}\frac{\partial w}{\partial\eta}\right)\right]-A_1\frac{\partial}{\partial\eta}(\rho vw)+\frac{A_2}{r}\frac{\partial}{\partial\eta}(\rho ww) -\mu\left[-\frac{1}{r}\frac{\partial}{\partial r}\left(A_1 r\frac{\partial w}{\partial\eta}\right)-A_1\frac{\partial}{\partial\eta}\left(\frac{\partial w}{\partial r}\right) +\frac{A_1^2}{\eta}\frac{\partial}{\partial\eta}\left(\eta\frac{\partial w}{\partial\eta}\right)+\frac{1}{r^2}\frac{\partial}{\partial\theta}\left(A_2\frac{\partial w}{\partial\theta}\right) +\frac{A_2}{r^2}\frac{\partial}{\partial\eta}\left(\frac{\partial w}{\partial\theta}\right)+\frac{A^2}{r^2\eta}\frac{\partial}{\partial\eta}\left(\eta\frac{\partial w}{\partial\eta}\right)\right]. \tag{A.3}$$

Continuity:

$$\frac{1}{r}\left[\frac{\partial}{\partial\theta}(\rho u)+\frac{\partial}{\partial r}(\rho rv)+\frac{1}{\delta}\frac{\partial}{\partial\eta}(\rho rw)\right]+A_2\frac{\partial}{\partial\eta}(\rho u) -A_1\frac{\partial}{\partial\eta}(\rho v)=0. \tag{A.4}$$

In the previous equations the following quantities were introduced:

$$A_1=\frac{\eta}{\delta}C_2\cos\theta,\quad A_2=\frac{\eta}{\delta}rC_2\sin\theta,\quad C_2=-\tan\alpha.$$

References

Demuren, A.O., Wilson, R.V., 1993. Estimating uncertainty in computation of two-dimensional separated flows. ASME Journal of Fluids Engineering 116, 216–221.

Ervin, J.S., Suryanarayana, N.V., Ng, H.C., 1989. Radial, turbulent flow of a fluid between two coaxial disks. ASME Journal of Fluids Engineering 111, 378–383.

Hayase, T., Humphrey, J.A.C., Grief, R., 1992. A consistently QUICK scheme for fast and stable convergence using finite-volume iterative calculation procedures. Journal of Computational Physics 98, 108–118.

Hayashi, S., Matsui, T., Ito, T., 1975. Study of flow and thrust in Nozzle–Flapper valves. ASME Journal of Fluids Engineering 97, 39–50.

Faghri, M., Sparrow, E.M., Prata, A.T., 1984. Finite difference solutions of convection/diffusion problems in irregular domain using a non-orthogonal coordinate transformation. Numerical Heat Transfer 7, 183–209.

Ferreira, R.T.S., Deschamps, C.J., Prata, A.T., 1989. Pressure distribution along valve reeds of hermetic compressors. Experimental Thermal and Fluid Sciences 2, 201–207.

Ferreira, R.T.S., Driessen, J.L., 1986. Analysis of the influence of valve geometric parameters on the effective flow and force areas. In: Ninth Purdue Compressors Technology Conference West Lafayette, USA, pp. 632–646.

Ferziger, J.H., Peric, M., 1996. Computational Methods for Fluid Dynamics. Springer, Berlin.

Gasche, J.L., Ferreira, R.T.S., Prata, A.T., 1992. Pressure distributions along eccentric circular valve reeds of hermetic compressors. In: Proceedings of the International Compressor Engineering Conference at Purdue West Lafayette, USA, IV, pp. 1189–1198.

Matos, F.F.S., Prata, A.T., Deschamps, C.J., 1999. Numerical analysis of the dynamic behavior of plate valves in reciprocating compressors. In: International Conference on Compressors and Their Systems. London, 13–15 September 1999, pp. 453-462.

Moffat, R.J., 1982. Contributions to the theory of single-sample uncertainty analysis. ASME Journal of Fluids Engineering 104, 250–260.

Patankar, S.V., 1980. Numerical Heat Transfer and Fluid Flow. Hemisphere, Washington, DC.

Prata, A.T., Ferreira, R.T.S, 1990. Heat transfer and fluid flow considerations in automatic valves of reciprocating compressors. In: Proceedings of the 1990 International Compressor Engineering Conference West Lafayette, USA, I, pp. 512–521.

Prata, A.T., Pilichi, C.D.M., Ferreira, R.T.S., 1995. Local heat transfer in axially feeding radial flow between parallel disks. ASME Journal of Heat Transfer 117, 47–53.

Prata, A.T., Sparrow, E.M., 1984. Heat Transfer and fluid flow characteristics for annulus of periodically varying cross section. Numerical Heat Transfer 7, 254–273.

Roache, P.J., 1993. A method for uniform reporting of grid refinement studies. In: Quantification of Uncertainty in Computation Fluid Dynamics, vol. 158. ASME FED, pp. 109–120.

Sparrow, E.M., Prata, A.T., 1983. Numerical solutions for laminar flow and heat transfer in a periodically converging-diverging tube with experimental confirmation. Numerical Heat Transfer 6, 441–461.

Tabatabai, M., Pollard, A., 1987. Turbulence in radial flow between parallel disks at medium and low Reynolds numbers. Journal of Fluid Mechanics 185, 483–502.

Wark, C.E., Foss, J.F., 1984. Forces caused by the radial outflow between parallel disks. ASME Journal of Fluids Engineering 106, 292–297.